

3-D electrical resistivity tomography using adaptive wavelet parameter grids

A. Plattner,^{1*} H.R. Maurer,¹ J. Vorloeper² and M. Blome³

¹Institute of Geophysics, ETH Zurich, Sonneggstrasse 5, 8092 Zurich, Switzerland. E-mail: plattner@alumni.ethz.ch

²Institute for Natural Sciences, Hochschule Ruhr West, Mülheim an der Ruhr, Germany

³Konrad-Zuse-Zentrum für Informationstechnik, Berlin (ZIB), Berlin, Germany

Accepted 2012 January 9. Received 2011 November 28; in original form 2011 March 14

SUMMARY

We present a novel adaptive model parametrization strategy for the 3-D electrical resistivity tomography problem and demonstrate its capabilities with a series of numerical examples. In contrast to traditional parametrization schemes, which are based on fixed disjoint blocks, we discretize the subsurface in terms of Haar wavelets and adaptively adjust the parametrization as the iterative inversion proceeds. This results in a favourable balance of cell sizes and parameter reliability, that is, in regions where the data constrain the subsurface properties well, our parametrization strategy leads to a fine grid, whereas poorly resolved areas are represented only by a few large blocks. This is documented with eigenvalue analyses and by computing model resolution matrices. During the initial iteration steps, only a few model parameters are involved, which reduces the risk that the regularization dominates the inversion. The algorithm also automatically accounts for non-linear effects caused by pronounced conductivity contrasts. Inside conductive features a finer grid is generated than inside more resistive structures. The automated parameter adaptation is computationally efficient, because the coarsening and refinement subroutines have a nearly linear numerical complexity with respect to the number of model parameters. Because our approach is not tightly coupled to electrical resistivity tomography, it should be straightforward to adapt it to other data types.

Key words: Wavelet transform; Inverse theory; Tomography; Electrical properties.

1 INTRODUCTION

Recovering the physical subsurface properties from surface-based geophysical measurements is a powerful means for improving our knowledge about the interior of the earth on a variety of scales. This is typically achieved with tomographic inversion techniques. In contrast to medical tomography, where transmitters and receivers can be conveniently placed around the target structure giving 360° view angle coverage, geophysical experiments usually have to resolve 3-D subsurface structures with an (at best) 2-D observation network at the Earth's surface and/or in a limited number of boreholes. This results in most geotomography inversion problems being ill-posed, meaning that there are many subsurface models that can explain the observed data equally well within a realistic noise range. This problem is particularly pronounced for potential field methods, such as electrical resistivity tomography (ERT) (e.g. Dey & Morrison 1979a,b; Spitzer 1995; Zhou & Greenhalgh 2001; Rücker *et al.* 2006).

There exist different strategies to counter this problem. One option is to impose regularization constraints. As outlined by Tarantola & Valette (1982), it is possible to include *a priori* information in the form of data and model covariance matrices, such that the resulting inversion problem has a unique solution. This is an extremely useful approach when sufficient *a priori* information about the subsurface exists, but it may produce misleading results when the assumptions and *a priori* information are insufficient and/or possibly flawed.

Another option for reducing the underdetermined aspect of the tomographic inversion problem is statistical experimental design. Here, survey layouts are identified which constrain the model parameters in an optimized fashion (e.g. Maurer *et al.* 2010, and the references therein). This proved to be very successful (e.g. Stummer *et al.* 2004), but even under the most favourable experimental setup, the poorly determined nature of the problem may be still substantial.

A third possibility for tuning the tomographic inversion is to optimize the model parametrization, such that its ill-determined component is minimized. This could be achieved by representing the subsurface structure with only a few model parameters, which have a high model resolution (defined in e.g. Menke 1989). However, this benefit comes at the expense of larger cell sizes. This well-known

*Now at: Department of Geosciences, Princeton University, Princeton, NJ, USA.

trade-off between a fine parameter grid and model resolution is discussed in many textbooks (e.g. Menke 1989) and renders optimized model parametrization to be a difficult task. One is typically interested in both a fine parameter grid and a high model resolution of the individual grid cells. This is not only the case for ERT, but also arises in many other tomographic problems. Therefore, the literature offers a wide variety of strategies for the choice of parametrization.

A possible parametrization strategy could be to initially choose a relatively coarse parametrization and to refine it adaptively during an iterative inversion. Alternatively, one may start with a very fine mesh and coarsen it adaptively. Several approaches have been proposed for controlled-source traveltome tomography (e.g. Michelini, 1995; Curtis & Snieder 1997; Bohm & Vesnaver 1999; Weber 2001; Trinks *et al.* 2005; Ajo-Franklin *et al.* 2006) and in local, regional and global earthquake tomography (e.g. Bijwaard *et al.* 1998; Chiao & Kuo 2001; Spakman & Bijwaard 2001; Sambridge & Faletic 2003; Nolet & Montelli 2005; Zhang & Thurber 2005; Tikhotsky & Achauer 2008; Simons *et al.* 2011). Other researchers have proposed adaptive model parametrizations that are suitable for ERT and induced polarization problems (e.g. Ascher & Haber 2001; Pessel & Gibert 2003; Haber *et al.* 2007). The literature also includes numerous applications to medical tomography and materials testing (e.g. Molinari *et al.* 2002; Kim *et al.* 2004; Rantala *et al.* 2006).

There exist several strategies for model refinement or coarsening. Bohm & Vesnaver (1999) propose to adapt the grid manually after each inversion step. Ascher & Haber (2001) start the inversion with a very coarse rectangular grid and then uniformly refine the grid with each iterative step. Refinement/coarsening can be performed with structured rectangular meshes, or other parametrization schemes, such as Delaunay triangulation (e.g. Ajo-Franklin *et al.* 2006) or Voronoi cells (e.g. Zhang & Thurber 2005). Finally, several authors have proposed parametrization schemes that are based on wavelets (e.g. Rantala *et al.* 2006; Tikhotsky & Achauer 2008; Simons *et al.* 2011).

A key element of each adaptive model parametrization algorithm is the measure by which it is decided where model refinement (or coarsening) should be performed. This measure should be generally capable of optimizing the trade-off between cell size and model resolution, but there are other requirements that need to be considered as well. For example, it is usually desirable that all model parameters are similarly well constrained. This is particularly critical for many surface-based geophysical measurements, where the model resolution per volume unit decreases rapidly with depth (e.g. Maurer & Boerner 1999). This requires an appropriate model coarsening with increasing depth. Finally, the computational efficiency of a refinement/coarsening measure must be ensured, such that it is applicable to large-scale 3-D problems.

Conceptually, the most powerful option for refinement/coarsening decisions would be to analyse the singular values of the sensitivity matrix or the eigenvalue spectra of the pseudo-Hessian matrix for a given model parametrization and given recording configuration. Because such approaches require repeated determinations of the singular/eigenvalues, this is computationally very expensive and therefore restricted to relatively small problems. As an alternative, Kim *et al.* (2004) performed electrical impedance tomography by starting with a fine grid and then grouped cells together with similar conductivities. Molinari *et al.* (2002) applied refinements to inversion cells having high conductivity gradients with adjacent cells. Haber *et al.* (2007) refined the grid where the model shows strong variations within a given functional. Michelini (1995) proposed to allow the position of the grid points to vary

during the inversion and additionally invert for these variations. This seems to work well for simple setups, but the method gets trapped easily in local minima for more complicated problems (Ajo-Franklin *et al.* 2006). In seismic traveltome tomography, it is common to approximate the parameter reliability with its ray hit count (e.g. Bijwaard *et al.* 1998) and make refinement/coarsening decisions such that all parameters are similarly well resolved.

Inspired by the ease with which wavelets can handle adaptivity, it has been investigated whether such techniques would also be suitable for inverse problems. The first attempts were made by Donoho (1995), who introduced the wavelet-vaguelette approach. This method works well for certain inverse problems, but the vaguelettes are generally not available in analytic form and must be calculated numerically. The approach by Cohen *et al.* (2004) overcomes this problem. They proposed an adaptive wavelet Galerkin method. Unfortunately, this approach is not applicable to typical geophysical inversion problems, because it assumes that the sensitivity matrix in the full wavelet basis has only non-zero singular values. Loris *et al.* (2007), Daubechies *et al.* (2008), Loris (2009) and Simons *et al.* (2011) employed wavelets to create sparsity promoting regularizations, but they did not erase those wavelets with small parameter coefficients from the basis and no refinement was performed.

In this contribution we transfer the adaptive wavelet approach presented in Cohen *et al.* (2003b) for well posed problems into the realm of underdetermined ERT. This requires new measures that control the automatic wavelet adaptation. The primary goal of this study is to improve the model reliability, not necessarily computational efficiency. Although we tailor our adaptive strategy to ERT, the method is expected to be applicable to other types of geophysical inversions. After a brief introduction to the theoretical background, we present details of the adaptive algorithm. Its features are investigated by eigenvalue and model resolution analyses. Finally, inversion results are compared with a non-adaptive state-of-the-art ERT algorithm.

2 FORWARD PROBLEM

The ERT forward problem is governed by the Poisson equation

$$-\nabla \cdot (\sigma \nabla u_s) = I \delta_s, \quad (1)$$

where σ is the electrical conductivity, u_s is the resulting total electric potential field, I the current source strength and δ_s the delta functional, which is non-zero only at the current injection point r_s . There exists a plethora of numerical methods for solving eq. (1) (e.g. Dey & Morrison 1979b; Rucker *et al.* 2006; Blome *et al.* 2009). In this study, we focus on the properties of the parameter adaptation and its effects on the quality of the inversion results. We do not explore the overall numerical performance in terms of computation time and memory requirements. In fact, our inversion parametrization scheme is independent of the numerical performance of the forward problem. It simply has to be ensured that the forward solution is sufficiently accurate. Here, we consider an adaptive wavelet forward solver presented by Plattner *et al.* (2010). This algorithm automatically generates forward modelling grids that are typically finer than the model parametrization grid.

Eq. (1) describes the absolute electrical potential that would be observed from a current injection at a single point r_s . In practice, potential differences between two potential electrodes are measured, and current injections are realized via a pair of electrodes. The response of such bipole–bipole configurations can be computed by superposition (e.g. Telford *et al.* 1990). For the sake of simplicity,

we restrict ourselves to pole–pole configurations, where the current sink and the reference potential electrode are placed at ‘infinity’, such that the data d_{ij} are the potentials u_i generated by a current injection (source) at electrode i and measured at electrode j with the pole–pole array. Nevertheless, the proposed inversion scheme is expected to be applicable to any other type of three- or four-electrode configuration.

3 INVERSE PROBLEM

Because solving equation $d^{\text{calc}} = \text{Forw}(m)$, described by eq. (1) ($m = \sigma$) for the parameter m is non-linear, we employ an iterative Gauss-Newton algorithm, which involves the solution of the linearized problem

$$G(m - m^0) = (d^{\text{obs}} - d^{\text{calc}}), \quad (2)$$

where m^0 is the input model, G the Jacobian matrix containing the Fréchet derivatives (also called sensitivities) of Forw at m^0 . The calculation of G requires that the partial derivatives of the data with respect to the model parameters to be determined. This can be done most elegantly using a perturbation approach. In the following i represents the source electrode index, j denotes the receiver electrode index and k is the conductivity parameter index. For a simulated measurement d_{ij}^{calc} , the partial derivative at a particular point r in the space domain Ω can be written as

$$g_{ij}(r) := \frac{\partial d_{ij}^{\text{calc}}}{\partial m(r)} = -\frac{1}{I} \nabla u_i(r) \cdot \nabla u_j(r) \quad (3)$$

(e.g. Zhou & Greenhalgh 1999), where I is the injection current strength and u_i and u_j are the electrical potentials that are observed at position r if the current is injected at electrodes i (true source) and j (adjoint source, or receiver position), respectively.

For a representation of the subsurface in the form of a linear combination of a finite number of orthogonal basis functions $\phi_k(r)$, we can write the derivative with respect to the k th basis function by means of the inner product of $g_{ij}(r)$ with $\phi_k(r)$

$$G_{ij}^k := \frac{\partial d_{ij}^{\text{calc}}}{\partial m_k} = \int_{\Omega} g_{ij} \phi_k dr. \quad (4)$$

Typically, ERT models are discretized in form of disjoint blocks, that is, $\phi_k(r)$ is constant within the k th block and 0 elsewhere. As discussed later, other types of model parametrization are possible as well.

Because the electrical potentials as well as the subsurface conductivities can vary over several orders of magnitude, and both quantities are strictly positive, the problem is usually formulated using logarithmic quantities (e.g. Tarantola 2005).

$$\tilde{G}_{ij}^k := \frac{\partial \tilde{d}_{ij}^{\text{calc}}}{\partial \tilde{m}_k} := \frac{\partial \log(d_{ij}^{\text{calc}})}{\partial \log(m_k)} = \frac{m_k}{d_{ij}^{\text{calc}}} G_{ij}^k \quad (5)$$

(the symbol $\tilde{\cdot}$ denotes log quantities). Usually, neither eq. (2) nor its least squares formulation

$$\tilde{m}^1 = \underset{\tilde{m}}{\text{argmin}} (\|\tilde{G}(\tilde{m} - \tilde{m}^0) - (\tilde{d}^{\text{calc}} - \tilde{d}^{\text{obs}})\|^2) \quad (6)$$

can be solved because the condition number of the matrix \tilde{G} is very high or even infinite. Therefore, we must supply regularization constraints in the form of damping and smoothing

$$\tilde{m}^1 = \underset{\tilde{m}}{\text{argmin}} (\|\tilde{G}(\tilde{m} - \tilde{m}^0) - (\tilde{d}^{\text{calc}} - \tilde{d}^{\text{obs}})\|^2 + \lambda \|\tilde{m} - \tilde{m}^0\|^2 + \gamma \|C\tilde{m}\|^2), \quad (7)$$

where C is a Laplacian smoothing matrix. The parameters λ and γ allow the influence of the regularization to be tuned (e.g. Maurer *et al.* 1998). Calculating the gradient of this minimization problem in eq. (7) and setting it zero leads to an improved estimate of the model parameters \tilde{m}^1

$$\tilde{m}^1 = (\tilde{G}^t \tilde{G} + \lambda I + \gamma C^t C)^{-1} [\tilde{G}^t (\tilde{d}^{\text{calc}} - \tilde{d}^{\text{obs}}) + \tilde{G}^t \tilde{G} \tilde{m}^0 + \lambda \tilde{m}^0] \quad (8)$$

(e.g. Tarantola 2005). For the next iteration, \tilde{m}^0 is set to \tilde{m}^1 and the procedure is repeated until convergence is achieved, and/or the average difference between observed and calculated data reaches the noise level.

Our algorithm, described in more detail in Section 5, differs in two ways from traditional inversion schemes. First, we do not discretize the model domain Ω with discrete blocks, but we employ a wavelet parametrization described in Section 4. Furthermore, we adaptively modify the choice of wavelets to represent the subsurface.

4 WAVELET BASIS FUNCTIONS

Wavelets were originally introduced by the French geophysicist Jean Morlet in the late 1970s (Daubechies 1996). Soon, the mathematical community discovered the wide applicability of this concept including, but not limited to, image compression (e.g. Brislawn *et al.* 1996), data analysis (e.g. Holschneider 1995), numerical partial differential and integral equations (Cohen *et al.* 2003b), inverse problems (Cohen *et al.* 2004) and compressed sensing (Cohen *et al.* 2009).

In image compression, the storage of high-resolution images using pixel-based storage schemes (i.e. using small-support basis functions) may result in excessively large data volumes. Wavelets allow the representation of the digital images with large-support basis functions, which may extend over larger areas of the domain of interest, and only a few small-support basis functions, which characterize the small-scale details. A key feature of such image compression schemes is the consideration of the image complexity, such that an image with only a few structural details can be stored more compactly than a more complex image. There exists a large variety of different wavelet families (e.g. Daubechies 1992), and a proper choice is problem dependent. Here, we adapt the concept of image compression using wavelet basis functions to model parametrization in geophysical inversion problems.

Because many subsurface structures are expected to be piecewise constant, we judge it appropriate to represent the model space using Haar wavelets. Every wavelet basis comprises scaling functions and wavelets. Scaling functions represent the average value of a function over a region. The size of the region depends on the starting level of the wavelet basis. 1-D scaling functions on the unit interval $[0, 1]$ are defined as

$$\phi_{l_0, p}^{1-D}(x) := \begin{cases} 2^{-l_0/2} & \text{if } 2^{-l_0} p \leq x < 2^{-l_0}(p+1), \\ 0 & \text{else,} \end{cases} \quad (9)$$

where the integer l_0 is the starting level and the integers $0 \leq p \leq 2^{-l_0}$ the positions of the scaling functions. To be able to represent nonzero values at $x = 1$, the scaling function for $p = 2^{-l_0} - 1$ has value $2^{-l_0/2}$ at $x = 1$.

Wavelets describe structural details that are not captured by the scaling functions. They exist on levels equal to or greater than the starting level l_0 . For any level $l \geq l_0$, 1-D Haar wavelets for positions

$0 \leq p < 0.5 \times 2^{-l}$ are defined as

$$\psi_{l,p}^{1-D}(x) := \begin{cases} 2^{-l/2} & \text{if } 2^{-(l+1)}2p \leq x < 2^{-(l+1)}(2p+1), \\ -2^{-l/2} & \text{if } 2^{-(l+1)}(2p+1) \leq x < 2^{-(l+1)}(2p+2), \\ 0 & \text{else.} \end{cases} \quad (10)$$

For positions $0.5 \times 2^{-l} \leq p < 2^{-l} - 1$, the wavelets are defined as

$$\psi_{l,p}^{1-D}(x) := \begin{cases} -2^{-l/2} & \text{if } 2^{-(l+1)}2p \leq x < 2^{-(l+1)}(2p+1), \\ 2^{-l/2} & \text{if } 2^{-(l+1)}(2p+1) \leq x < 2^{-(l+1)}(2p+2), \\ 0 & \text{else.} \end{cases} \quad (11)$$

The wavelets for $p = 2^l - 1$ have the value $2^{-l/2}$ for $x = 1$.

3-D scaling functions can be constructed via tensor products and are defined as the linear span of the functions

$$\varphi_{l_0,p_x,p_y,p_z}(x,y,z) = \varphi_{l_0,p_x}^{1-D}(x) \cdot \varphi_{l_0,p_y}^{1-D}(y) \cdot \varphi_{l_0,p_z}^{1-D}(z).$$

Hence, they form disjoint cubes. Similarly, 3-D wavelets are defined as the span of the following types of functions

$$\psi_{l,p_x,p_y,p_z}(x,y,z) = (\phi_{l,p_x}^{(a)})^{1-D}(x) \cdot (\phi_{l,p_y}^{(b)})^{1-D}(y) \cdot (\phi_{l,p_z}^{(c)})^{1-D}(z), \quad (12)$$

where $\phi^{(a)}$, $\phi^{(b)}$ and $\phi^{(c)}$ are replaced by either φ or ψ . However, at least one of the three factors needs to be of type ψ (otherwise the tensor product is a scaling function). Therefore, for each level and position there exist seven different wavelets, whereby each of these wavelets is associated with a model parameter that may be included in vector \tilde{m} .

A 1-D Haar wavelet basis is depicted schematically in Fig. 1. The log conductivity model can be parametrized as a linear combination of Haar scaling functions and wavelets, whereby the model vector includes the coefficients of the scaling functions and wavelets chosen

$$\sigma(r) = \sum_{k=1}^{\text{NSF}} \tilde{m}_k \varphi_k(r) + \sum_{k=\text{NSF}+1}^{\text{NSF}+\text{NW}} \tilde{m}_k \psi_k(r) = \sum_{k=1}^{\text{NSF}+\text{NW}} \tilde{m}_k \phi_k(r), \quad (13)$$

where NSF is the number of scaling functions and NW the number of wavelets selected. The single index k stands for the multiindex containing level and position, and in the 2-D or 3-D cases also for the wavelet type. A schematic 1-D example for the summation in eq. (13) is shown in Fig. 2.

5 ALGORITHM DESCRIPTION

Fig. 3 outlines the concept of our approach and algorithm *AdaptiveInversion* at the end of this Section provides the mathematically more detailed description. The concept of our adaptivity is closely related to the adaptive wavelet solver described in Cohen *et al.* (2003b). We make use of the refinement procedure applied therein, which is described in more detail in Cohen *et al.* (2003a). In contrast to well-posed problems, where the algorithm was proven to provide quasi-optimal grids for a wide range of problems, we can not prove that this also holds for the ill-posed ERT. Rather, we make use of concepts that were successful in well-posed problems and apply them to an ill-posed setting as part of a heuristic. To show the performance of our scheme, we provide numerical examples.

The algorithm is initialized by specifying the modelling domain Ω , choosing an appropriate starting model m_0 and selecting suitable regularization parameters. The initial model parametrization includes all scaling functions and a choice of wavelets. Appropriate conductivity values are assigned to the corresponding wavelet

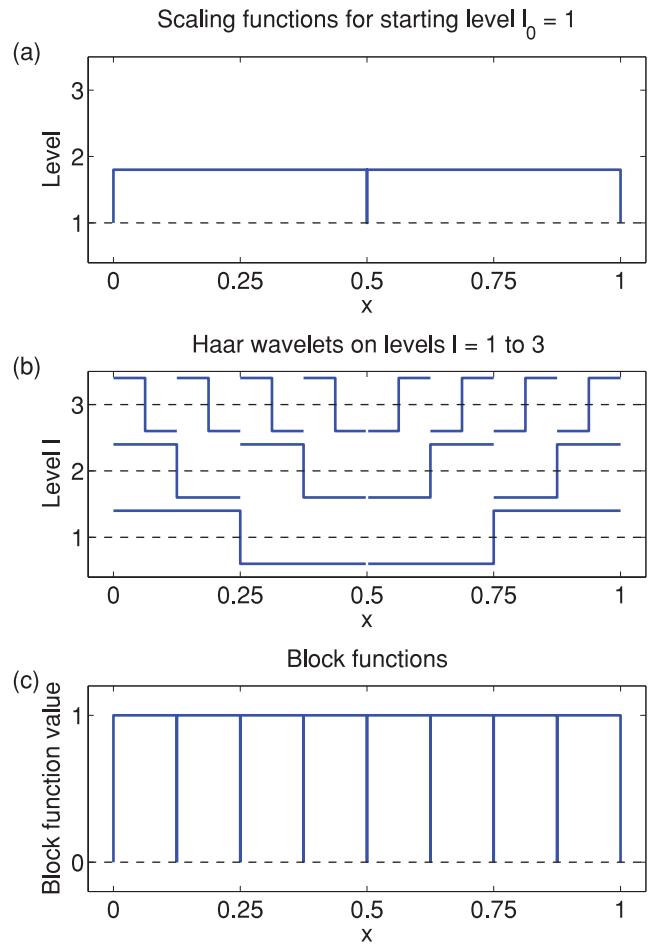


Figure 1. Examples of 1-D model parametrizations. (a) Haar scaling functions at level 1. (b) All Haar wavelets from level 1 to 3. (c) Piecewise constant block functions for an equivalent resolution as the Haar wavelet basis up to level 2.

coefficients. Then, the forward problem is solved for this conductivity structure and given set of electrode configurations and the sensitivities are computed.

Some of the model parameters (i.e. the wavelet coefficients) are expected to be well resolved, whereas others may be only poorly constrained by the data. Identification of poorly constrained coefficients requires a measure for the parameter reliability. A possible option would be to consider the diagonal elements of the model resolution matrix (e.g. Menke 1989). Unfortunately, this is computationally very expensive for large-scale inversion problems. A computationally less demanding alternative is the following. For each model parameter k we sum up the absolute values of the entries of the k th column of \tilde{G} . This sum can be interpreted as follows. The absolute value of a single entry \tilde{G}_{ij}^k in the sensitivity matrix \tilde{G} describes how strongly a change in datum ij can affect the model coefficient for parameter wavelet k . Therefore the sum of the absolute values of \tilde{G}_{ij}^k describes the general cumulative effect of changes in the data on the k th parameter coefficient. We therefore interpret this cumulative sensitivity for k as a suitable measure of the resolvability and importance of a single wavelet parameter k . Subsequently, we refer to this measure as ‘cumulative wavelet sensitivities’

$$(C_w)_k := \sum_{ij} |\tilde{G}_{ij}^k|. \quad (14)$$

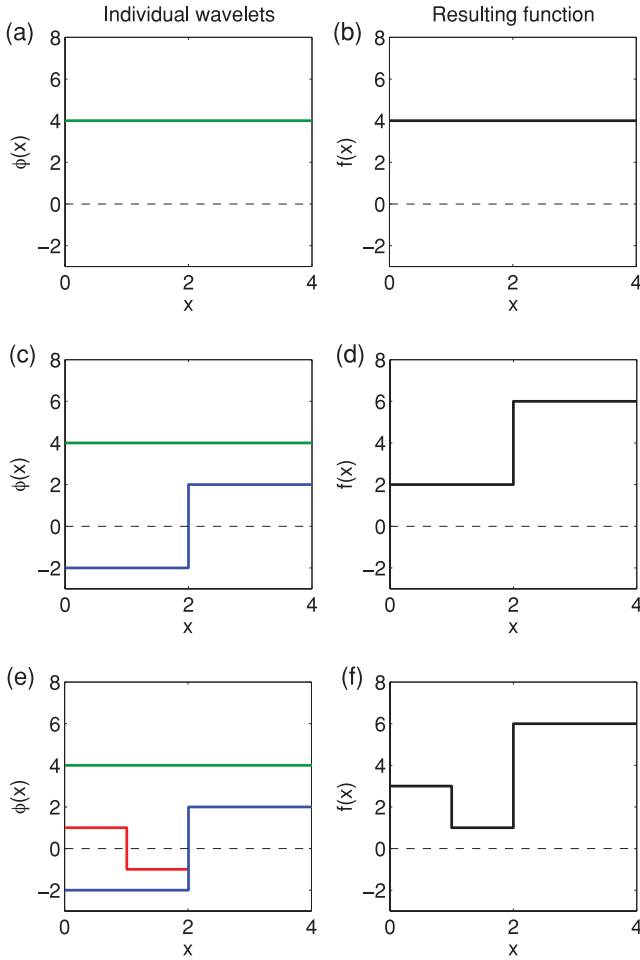


Figure 2. Example of a superposition of Haar wavelet basis functions to represent a piecewise continuous function. (a), (c) and (e) show the individual wavelet basis functions, (b), (d) and (f) show the piecewise constant function obtained by the summation of the wavelet basis functions on their left.

During the coarsening step (Fig. 3), those wavelet coefficients whose cumulative wavelet sensitivities are below a user defined threshold are removed. To ensure that the model representation in the Haar wavelet basis can be properly transformed into a block basis (disjoint blocks), the hierarchical wavelet trees (Fig. 1) have to be complete in the sense that for each wavelet the spatially overlapping lower or equal level wavelets and scaling functions are also included in the tree. This may require reinsertion of certain wavelets after the coarsening step. The equivalence between the choice of wavelets and a block basis is particularly useful for the setup of the smoothing matrix in eq. (7). We have based our implementation on an algorithm that uses a tree structure (Cohen *et al.* 2003b). Implementations without tree structures are also conceivable as for example, in the case of elliptic linear problems (Cohen *et al.* 2001).

Next, two independent tasks are scheduled, namely a model update and a model refinement (Fig. 3). The model update is straightforward and performed by evaluating eq. (8) using the coarsened model and the coarsened sensitivity matrix, which is obtained by deleting the corresponding columns of \tilde{G} .

The model refinement is more complicated. It follows closely the procedure described in Cohen *et al.* (2003a) and applied in Cohen *et al.* (2003b). Based on a measure that is similar to the cumulative wavelet sensitivities, our refinement procedure seeks

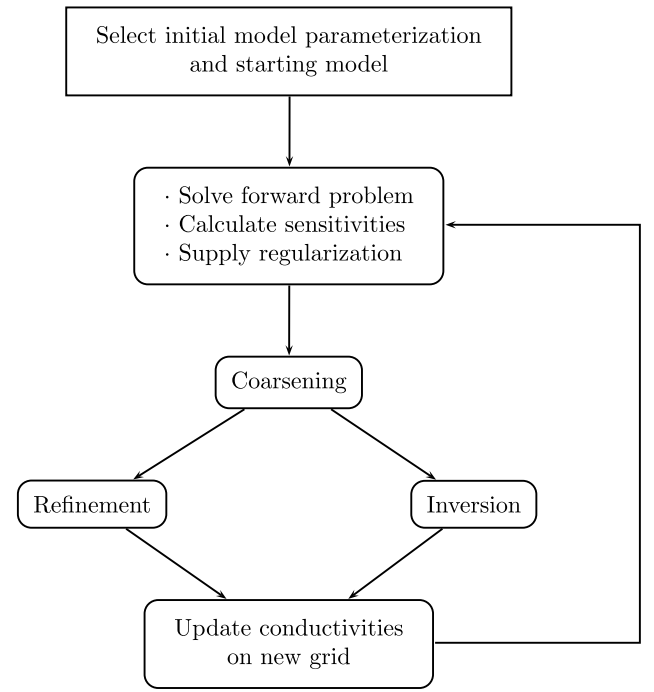


Figure 3. Flowchart of the algorithm. The refinement and inversion steps are performed independently and the results merged afterwards. The iteration is performed until convergence is achieved.

wavelets that are potentially well resolved. As for the coarsening, it has to be ensured that the refined branches of the wavelet tree remain complete. More details on the refinement procedure are provided in Appendix A.

After performing the model parameter updates and the model refinement, the results of these two tasks are merged by appending the newly chosen wavelets to the updated model with coefficients equal to zero, such that a new set of basis functions is available. With this new model parametrization and the updated model values, the forward problem and the associated sensitivities are recomputed, and the procedure is iterated until convergence is achieved.

Algorithm *AdaptiveInversion*($\Phi^{(0)}$, $\tilde{m}^{(0)}$, ε^c , ε^r)

Input: Starting parametrization, starting model, coarsening percentages, refinement parameter

Output: Inversion result model, wavelet parametrization

1. Set $t = 0$ and $(d_{ij}^{\text{calc}})^{(-1)} = \infty$.
2. **While** $\|d^{\text{obs}} - (d^{\text{calc}})^{(t-1)}\| > \delta$ **and** $t < t_{\text{max}}$.
3. **Do** Solve eq. (1) for $\sigma = m^{(t)}$ and for all i to obtain the $u_i(r)$.
4. Calculate $\tilde{G}^{(t)}$ using eqs (4) and (5).
5. $[\tilde{\Phi}^{(t)}, \tilde{m}^{(t)}, \tilde{G}^{(t)}] = \text{Coarse}(\tilde{G}^{(t)}, \tilde{m}^{(t)}, \Phi^{(t)}, \varepsilon_i^c)$.
6. Calculate $\tilde{m}^{(t+1)}$ by solving eq. (8) using $\tilde{G}^{(t)}$, $\tilde{m}^{(t)}$ and the Laplacian smoothing matrix $C(\tilde{\Phi}^{(t)})$.
7. Calculate the refinement $\hat{\Phi}^{(t+1)}$ as described in Appendix using $\tilde{G}^{(t)}$ as a measure for where and ε_i^r as a measure for how much to refine.
8. Set $\tilde{m}^{(t+1)} := \tilde{m}^{(t+1)}|_{\hat{\Phi}^{(t+1)}}$ (i.e. expand the entries of $\tilde{m}^{(t+1)}$ to $\hat{\Phi}^{(t+1)}$ by padding with zeros).
9. $t = t + 1$.
10. **return** $\tilde{m}^{(t)}$, $\tilde{\Phi}^{(t-1)}$.

Algorithm $Coarse[\tilde{G}, \tilde{m}, \Phi, \varepsilon]$

Input: Sensitivity matrix, model, wavelet basis, coarsening percentage.

Output: Coarsened wavelet basis, coarsened conductivity model, coarsened sensitivity matrix

1. Calculate C_w as described in eq. (14).
2. Sort C_w in descending order.
3. Set $K := 1$ and $\tilde{C}_w := \emptyset$.
4. **While** $\sum_{k=1}^K (C_w)_k < \|C_w\|^2(1 - \varepsilon^2)$.
5. **Do** Append $(C_w)_K$ to \tilde{C}_w .
6. $K = K + 1$
7. Set $\tilde{\Phi}$ as the wavelets, whose coefficients are in \tilde{C}_w and make $\tilde{\Phi}$ a complete tree.
8. Set $\tilde{m} := \tilde{m}|_{\tilde{\Phi}}$ and $\tilde{G} := \tilde{G}|_{\tilde{\Phi}}$.
9. Return $\tilde{\Phi}, \tilde{m}, \tilde{G}$.

6 NUMERICAL EXPERIMENTS

To demonstrate the behaviour and performance of our adaptive model refinement algorithm, we set up a hypothetical 10×10 electrode array (4.66 m electrode spacing) located on the top face of a cube with side length 140 m (Fig. 4). Only pole–pole configurations are considered. With 100 electrodes, $(100 \times 99)/2 = 4950$ independent pole–pole measurements can be simulated. To mimic a realistic surface-based ERT, Neumann (no normal component current flow) boundary conditions are imposed at the top face of the cube, and mixed boundary conditions (Dey & Morrison 1979b) are applied at the other faces. All conductivity values are displayed as resistivity $1/\sigma$ in Ωm . Four different conductivity models are considered, namely a homogeneous model with $100 \Omega m$, a single resistive or conductive block embedded in a homogeneous half space (Fig. 4a) and a more complicated four block model (Fig. 4b).

A wavelet parametrization includes overlapping scaling functions and wavelets at different levels, which are difficult to visualize. Because the coarsening and refinement procedures, described in Section 5 and Appendix A, ensure the completeness of the hierarchical wavelet trees, it is always possible to apply a wavelet transform and to display the model parametrization in the form of disjoint blocks, as shown for example in Fig. 5.

In our initial experiments, we employ the homogeneous model and perform an adaptive refinement without carrying out an inversion, that is, the true homogeneous model is retained for all computations and only coarsening and refinement are performed. Our initial model includes all scaling functions and wavelets at level 1, which is equivalent to an equally sized $4 \times 4 \times 4$ block parametrization. For the first iteration, we set the coarsening threshold ε_0^c to 5 per cent of the initial cumulative wavelet sensitivities norm (eq. 14). In each later step, the initial threshold ε_0^c is multiplied by 0.5^q , where q is the difference between the initial maximum level and the current maximum level.

The refinement procedure was initially carried out without constraining the maximum wavelet level, but experiments indicated that slightly more stable results can be achieved when an upper limit is imposed. We have chosen a maximum level of $l = 6$ (eqs 10 and 11), but this constraint does not seem to be very critical. The coarsening threshold strategy described earlier, and the process of restricting the maximum wavelet level during the refinement procedure was retained for all experiments presented in this section.

Figs 5(a) and (b) show horizontal and vertical slices through the resulting equivalent parameter grid after the first coarsening. Figs 5(c) and (d) show the parametrization after the consecutive refinement, recalculation of the sensitivities and coarsening. As expected, additional wavelets that characterize more detailed structures right underneath the electrode array (denoted by the red square

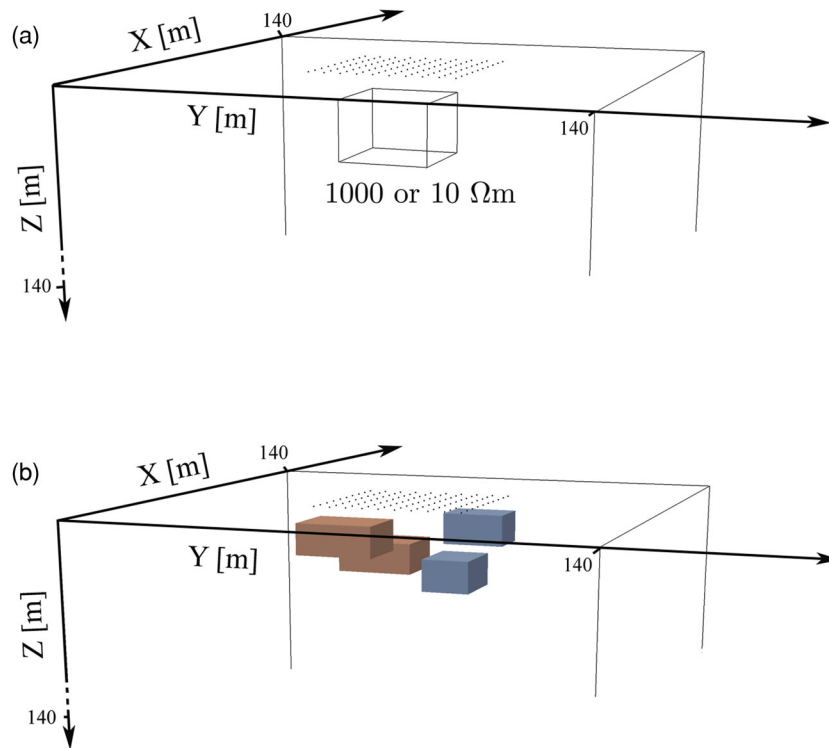


Figure 4. The three subsurface conductivity contrast models considered in this paper. (a) Experiment setup with the 10×10 electrodes on the surface and a background resistivity of $= 100 \Omega m$. The subsurface block resistivity is 10 or $1000 \Omega m$ for the different experiments. (b) Setup for the four block model. The red blocks have a resistivity of $1000 \Omega m$, and the blue blocks have $10 \Omega m$. The background resistivity is $100 \Omega m$.

in the horizontal and the red double-arrow in the vertical slices) are added. Further iteration steps Figs 5(e)–(h) continue to refine the model underneath the array. At greater depth, where the model resolution per volume unit is expected to be poor, the coarse parametrization structure is retained. It is also worth mentioning that there is a significant amount of refinement outside of the array. This is in accordance with the results of Maurer & Friedel (2006), who highlighted the importance of the ‘outer space’ and the fact that pole–pole configurations have particularly high sensitivities outside of the electrode grid.

Table 1 summarizes the development of the number of model parameters in the course of the iteration steps. After step 5, the number of parameters no longer increases significantly, but it starts oscillating

Table 1. Number of wavelet basis functions in each step for the homogeneous conductivity iteration without inversion.

| Step | After coarsening |
|------|------------------|
| 0 | 36 |
| 1 | 64 |
| 2 | 260 |
| 3 | 813 |
| 4 | 2962 |
| 5 | 9479 |
| 6 | 6847 |
| 7 | 9185 |
| 8 | 6903 |
| 9 | 9129 |

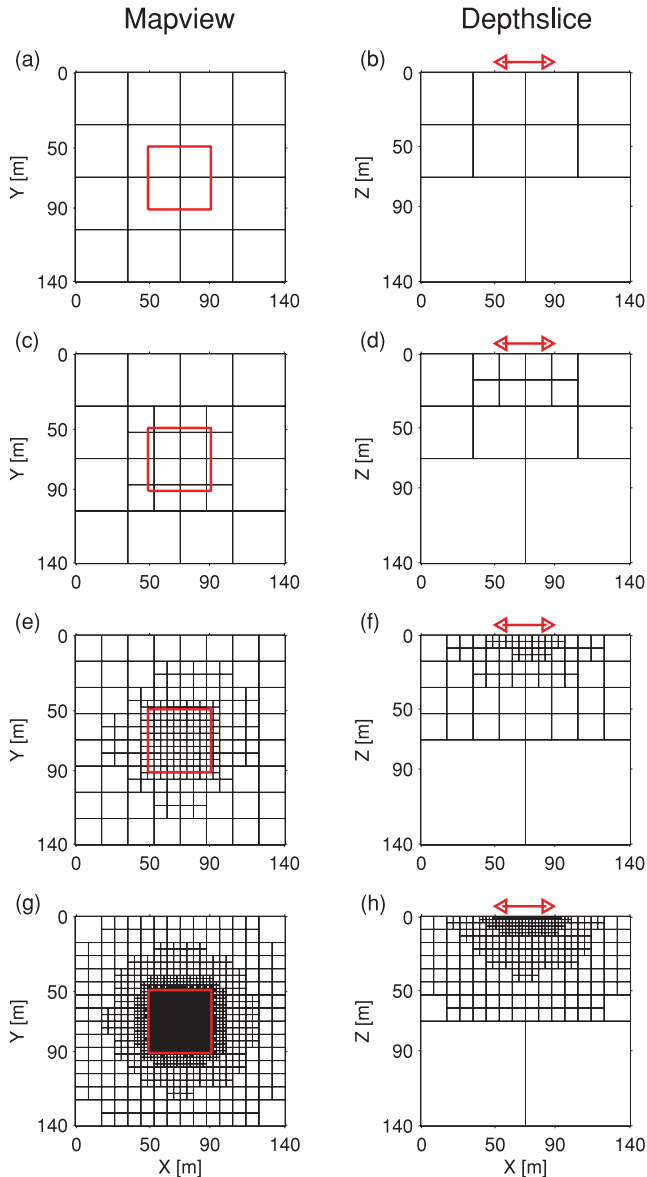


Figure 5. Resulting grids from the homogeneous conductivity iteration without inversion after coarsening. (a),(c),(e) and (g) show the grid on the surface with the electrode array indicated by the red square. (b), (d), (f) and (h) show slices through the grids perpendicular to the Y -axis at $Y = 70$. The electrode array is indicated by the red arrow. (a) and (b) show the grid after coarsening in step 0, (c) and (d) after coarsening in step 1, (e) and (f) after coarsening in step 3 and (g) and (h) after coarsening in step 5.

between about 7000 and 9000. The algorithm has apparently reached a level of refinement where several model parametrizations with similar properties exist. This can be further quantified with eigenvalue and model resolution analyses.

6.1 Eigenvalue analysis

More insights into the properties of the model parametrization can be gained from the eigenvalue spectra of the approximate Hessian matrix $\tilde{G}^T \tilde{G}$ related to the individual coarsening/refinement cycles (Fig. 3). Fig. 6(a) shows the eigenvalue spectra over the complete range of parameters, and Fig. 6(b) displays a close up of the most critical parts of the relative eigenvalue spectra. A desirable model parametrization exhibits a large number of eigenvalues that lie above a certain threshold (e.g. Blome *et al.* 2011). As can be seen in Fig. 6, this is achieved best for the eigenvalue spectra associated with iteration steps 5 to 9. These spectra almost coincide for relative eigenvalues $> 10^{-10}$, thereby indicating that the corresponding model parametrizations have a similar goodness.

6.2 Model resolution analysis

The eigenvalue spectra in Fig. 6 provide important information concerning the overall condition of the inverse problem, but it is difficult to judge which parameters are well resolved and which are not. This type of information can be obtained via the model resolution matrix R , which can be computed as

$$R = (\tilde{G}^T \tilde{G} + \lambda I + \gamma C^T C)^{-1} (\tilde{G}^T \tilde{G}) \quad (15)$$

(e.g. Menke 1989). At the initial stage of the inversion, the regularization parameters λ and γ are set to relatively high values, and in the course of the iterations they are continuously decreased down to a minimum value, which guarantees stable results. For computing R we have used a relatively small regularization strength with identical values for gamma γ and λ . The diagonal elements of R (subsequently referred to as the model resolution) indicate how well a parameter is resolved (0 = unresolved, 1 = perfectly resolved). In our model parametrization scheme the values of R are associated with individual scaling functions and wavelets, and a representation in the form of disjoint blocks is not meaningful. Fig. 7 therefore shows the average model resolutions grouped by wavelet levels contained in the individual model parametrizations after coarsening (Fig. 3). The scaling function resolution values are included in the wavelet level 1 resolution values.

Initially, only wavelets at level 1 are included. They are all relatively well resolved. After step 1, wavelets at levels 1 and 2 are

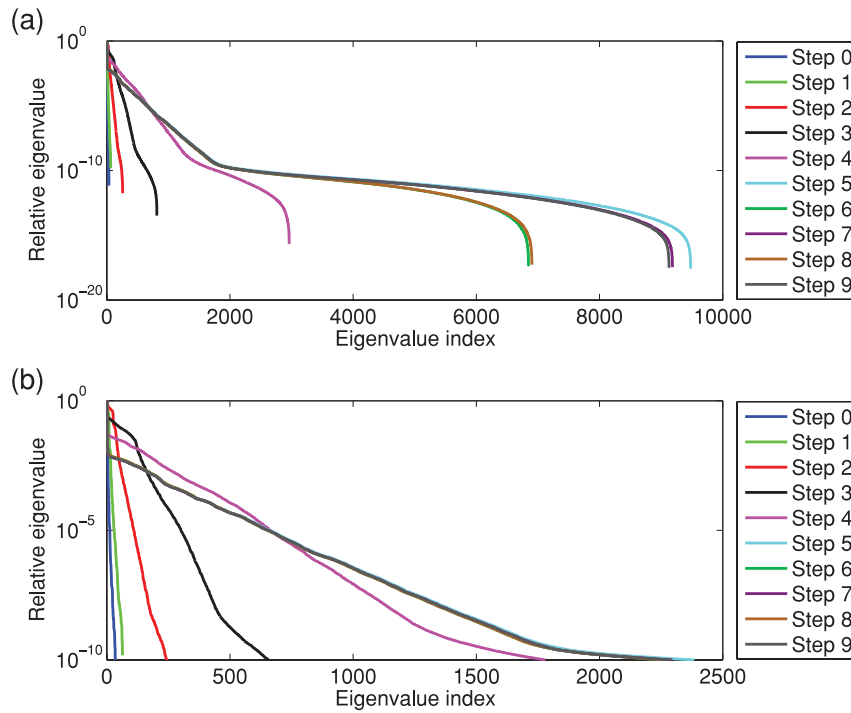


Figure 6. Relative eigenvalue spectra for the homogeneous conductivity iteration without inversion. The lower figure (b) is a zoom in of (a).

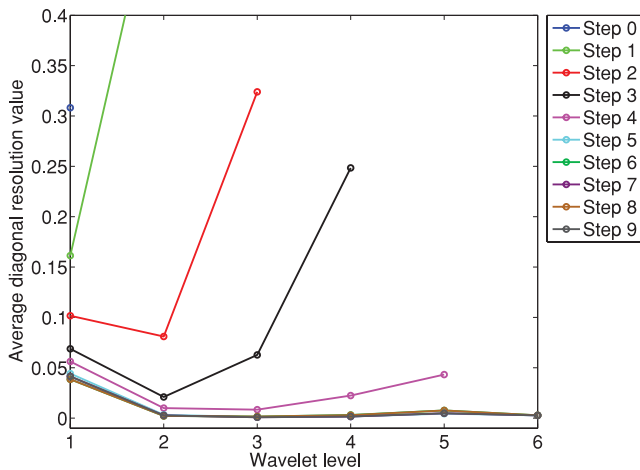


Figure 7. The diagonal entries of R in eq. (15). Each point in the diagram represents the average value of the diagonal entries for a given level.

considered. It is interesting to note that wavelets at level 2 have generally a better model resolution than those at level 1 and are even larger than those of the level 1 wavelets at the initial step 0. Furthermore, the model resolution at level 1 has decreased compared with the initial step 0. This observation can be explained as follows. Right beneath the electrodes, the model resolution is expected to be very good. The shallowest level 1 wavelets represent this well resolved range, but due to their relatively large spatial extension they also cover regions at greater depths, where the model resolution decreases rapidly. Therefore, their model resolution values represent an average over well-resolved and less well-resolved regions. After the first refinement step, wavelets at level 2 are added. They have smaller spatial extensions and cover only the very well resolved shallow regions. The decrease of the model resolution of the level 1

wavelets is the result of the increased number of model parameters that overlap in the well-resolved area.

Using a similar argumentation also allows the average model resolution values which result from the subsequent steps 2 to 9 to be explained (Fig. 7). It is important to note that the average model resolution values of the individual levels become more balanced for later iteration steps. This indicates that our algorithm performs as desired: the model resolutions become more balanced throughout the entire model, which suggests a good compromise concerning the trade-off between cell size and model resolution. In those regions where the model resolution is very high, the model parametrization has been refined, whereas the parametrization in regions with a poor model resolution remains at the initial stage.

6.3 Effects of conductivity contrasts

The sensitivity matrix \tilde{G} depends on the actual conductivity values. Hence, it is recalculated after each iterative step in our Gauss-Newton inversion algorithm. Because the coarsening and refinement procedures depend on the sensitivities, it is expected that these procedures are also affected by changing electrical conductivities. This is demonstrated in Fig. 8, which shows vertical cross-sections through the model parametrizations in the presence of an electrically conductive and resistive block (see Fig. 4(a) for the geometry of the anomalous block). As in the numerical experiments described earlier, we did not perform an actual inversion, but started with the $4 \times 4 \times 4$ grid, projected the conductivity onto this grid, calculated the sensitivities, coarsened and refined and then projected the conductivity onto the new grid. This was iterated five times. By omitting the update of the model after an inversion, we can isolate the effect of a conductivity contrast on the grid. Because the electrical currents preferably flow through the conductive block and tend to avoid the resistive block, the sensitivities inside of the block are expected to be larger for the former compared with the latter.

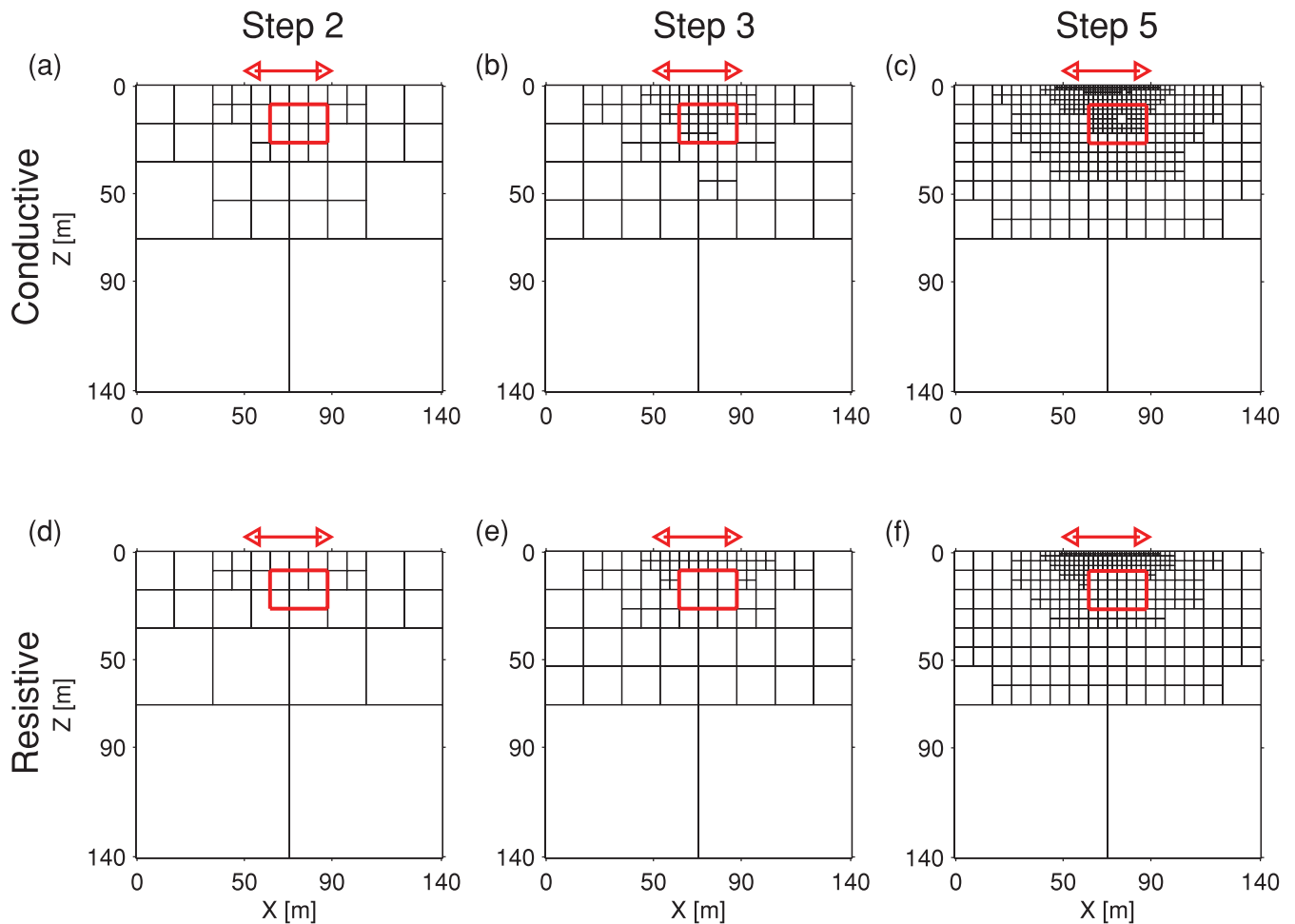


Figure 8. Vertical slices of resulting grids from the inhomogeneous conductivity iteration without inversion after coarsening. (a), (b) and (c) show the grids for the conductive block contrast and (d), (e) and (f) for the resistive box contrast displayed in Fig. 4(a). Here, the contrast is indicated by the red square and the electrode array by the red arrows. The grids are shown for step 2, 3 and 5.

This results in a coarser model parametrization inside the resistive block.

6.4 Inversion results

To demonstrate the applicability of our adaptive grids, we generated synthetic data for the three different subsurface models shown in Fig. 4. For checking the robustness of our approach, 2 per cent relative noise was added. In all cases, we chose the initial model parametrization to be as in step 3 from the first experiment (Figs 5e and f). The initial conductivities were set to the true background conductivity of $100 \Omega\text{m}$. Model reparametrization (coarsening and refinement) was performed only after every second Gauss-Newton inversion step.

Fig. 9 shows the results for the conductive and resistive block anomalies. As already observed in the previous experiment, shown in Fig. 8, the model parametrization is finer in conductive areas compared to resistive regions. The upper boundary of the conductive and resistive blocks are similarly well resolved, but since the current density is expected to be very small at the bottom of the resistive block, its lower boundary is less well resolved. The overall convergence behaviour for the two inversion runs is comparable. In both cases the rms dropped after seven iterations below the 2 per

cent error level. The resistive artefacts at larger depths in Fig. 9(b) are caused by the poor resolution of these parameters.

In a further test we considered the more challenging four block model, shown in Fig. 4(b). For testing the performance of the algorithm, we inverted the synthetic data with the algorithm presented in this paper and compared the results with a state-of-the-art inversion package described in Blome (2009) and Blome *et al.* (2010) (subsequently referred as ‘reference solution’). In the reference solution the model parametrization is obtained by a clustering of forward mesh cells with the help of an auxiliary staggered grid. The parametrization remains fixed throughout the entire inversion process, and the block sizes increase progressively with depth and in the horizontal direction (only outside of the electrode array area). To obtain best results for the reference solution, only the region beneath the array was allowed to vary, and the outer space regions were fixed to the true conductivities. We provided damping and smoothing and decreased their weighting with later inversion steps. The adaptive inversion was initialized with the grid from step 3 (Fig. 5). In contrast to the reference solution, model refinements and variations were allowed everywhere in the computation domain.

Comparisons of the inversion results are shown in Figs 11 and 12 by means of horizontal and vertical slices through the model volume as indicated in Fig. 10. At shallow levels ($<8 \text{ m}$), the reference solution obtained with the algorithm described in Blome (2009)

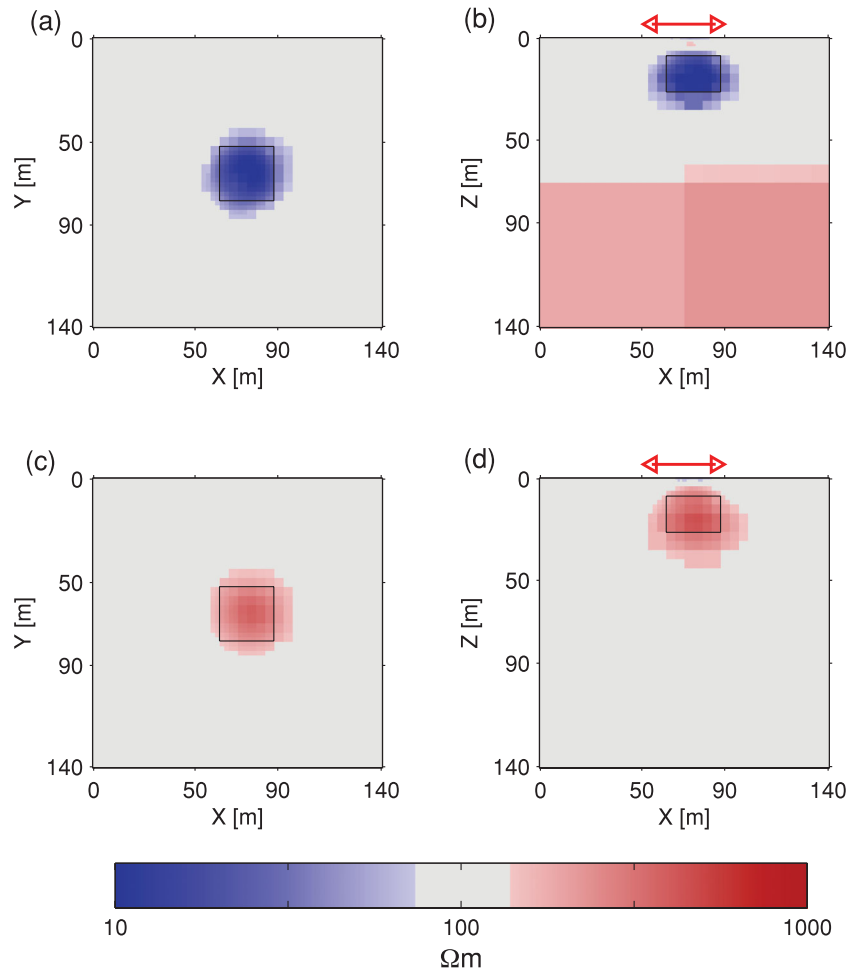


Figure 9. Inversion results for step 7 for the conductive [(a) and (b)] and resistive [(c) and (d)] contrasts displayed in Fig. 4(a). Panels (a) and (c) show a horizontal slice through the middle of the contrast at a depth of 17.5 m. Panels (b) and (d) show a vertical slice perpendicular to the Y -axis through the middle of the contrast at $Y = 66$ m. The red arrow indicates the electrode array. The conductivity contrast is indicated by the black box.

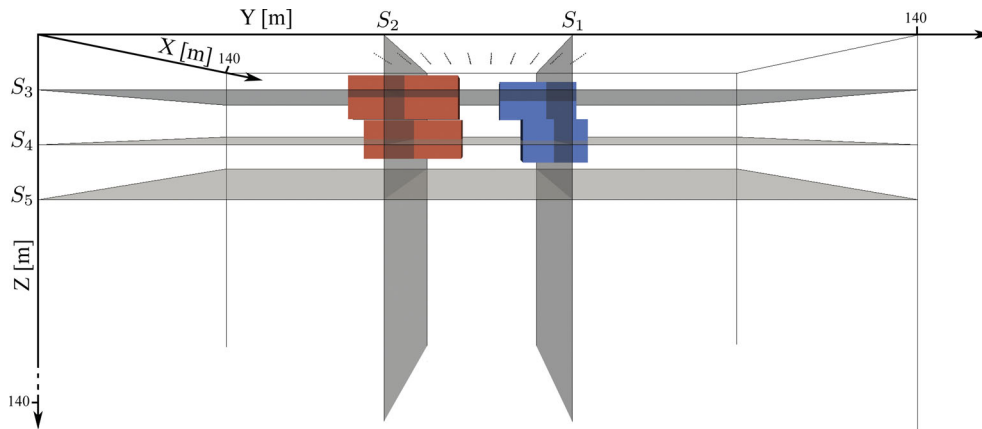


Figure 10. Sketch of slices through the four block model for which the inversion results are displayed in Figs 11 and 12.

produces slightly superior results (Figs 11a–c), but at deeper levels (Figs 11d–f) the adaptive algorithm (Fig. 11e) outperforms the reference solution (Fig. 11f). Although the adaptive algorithm produces rather blurred images of the four blocks, they are all clearly distinguishable in the tomographic reconstructions. By contrast, the deep-seated conductive block is hardly visible in the reference

solution (Figs 12e and f) and the resistive blocks appear as a single unit in Figs 11(f) and 12(f). Moreover, the reference solution exhibits pronounced artefacts at deeper levels (Figs 12e and f), which are probably the result of not well equilibrated resolutions of the inversion grid. The data rms curves for the reference solution and for the adaptive algorithm are displayed in Fig. 13. At step one,

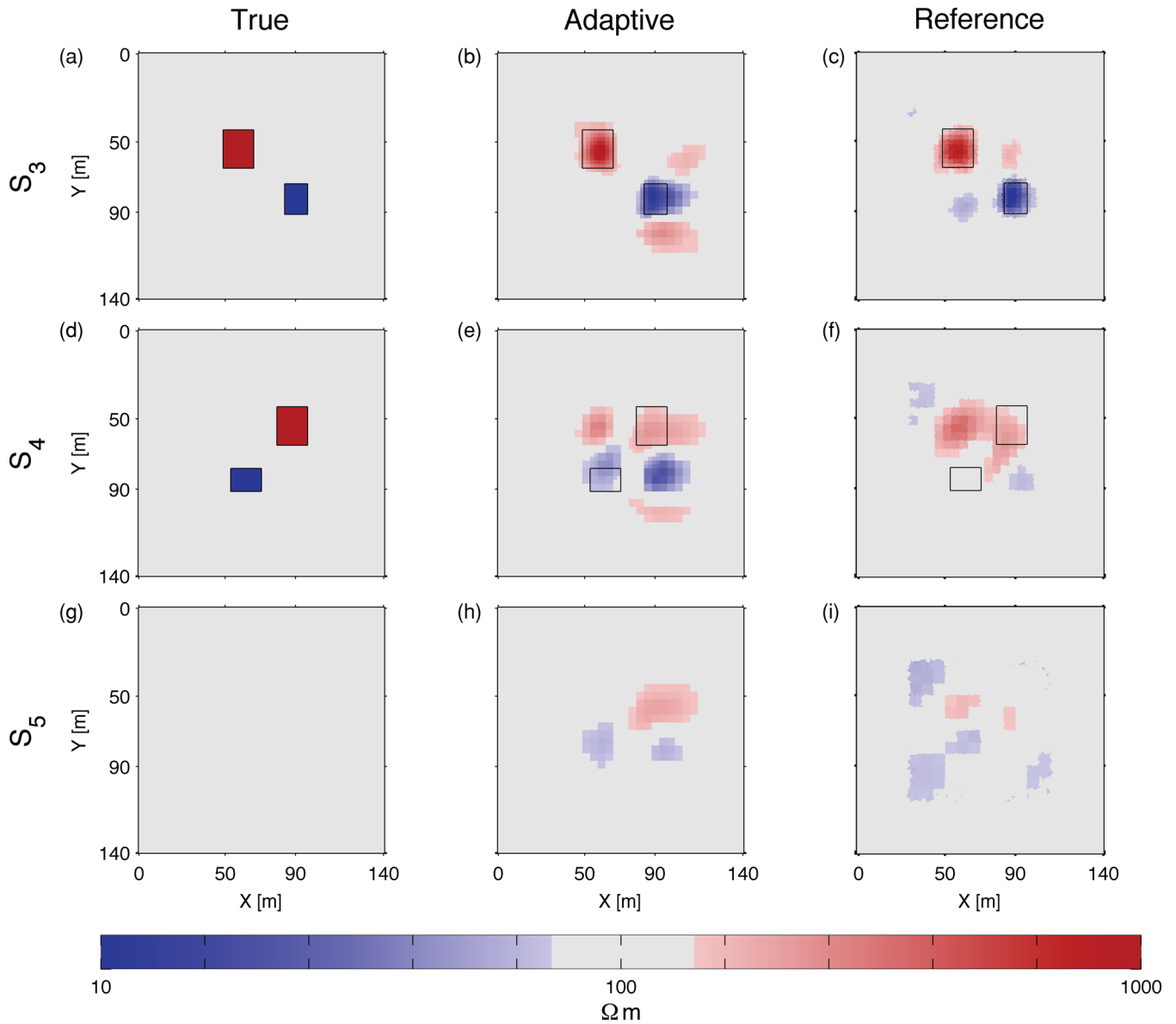


Figure 11. Horizontal slices indicated in Fig. 10 through the four block contrasts inversion results. Panels (a), (d) and (g) show the true model, panels (b), (e) and (h) the adaptive wavelet algorithm result and panels (c), (f) and (i) the reference solution. The different results are shown for slice S_3 in (a), (b) and (c), slice S_4 in (d), (e) and (f) and slice S_5 in (g), (h) and (i) (see Fig. 10). The contrast positions in each panel are indicated by the black boxes.

the reference solution better fits the observed data than the adaptive wavelet scheme but it does not improve much after step number three and stagnates above the noise level. However, the adaptive wavelet scheme steadily improves the rms misfit and reaches the noise level at step 7.

7 DISCUSSION AND CONCLUSIONS

We have presented a heuristic algorithm that automatically adapts the parameter grid in an ERT. Although we have no mathematical proof of the concept, we judge the results from our numerical tests to be promising. The main achievement of the new adaptive ERT algorithm is its capability to equilibrate the trade-off between cell size and model resolution. This allows the information content offered by a particular data set to be better exploited. Since the model parameters are automatically chosen such that the model

resolution remains acceptably good, it is necessary to supply only weak regularization constraints, which make the inversion result less dependent on possibly flawed *a priori* assumptions.

A further benefit of the presented algorithm is that it can automatically adapt the initial parameter grid to *a priori* information about the subsurface, if this information is included into the starting conductivity model. This can be done by choosing a coarse initial parametrization and then run the algorithm while retaining the conductivity values (i.e. only update the grid but not the conductivities). Although the parameter grid adaptation works well with a coarse grid, the conductivity update should be performed with a fine enough grid to avoid getting trapped in a local minimum. This is the reason why we have started our test inversions with grid number three in Fig. 5.

From eigenvalue and model resolution studies, as well as the inversion tests, we deem this algorithm to be beneficial. Besides its pure technical advantages we judge it also to be critical and desirable

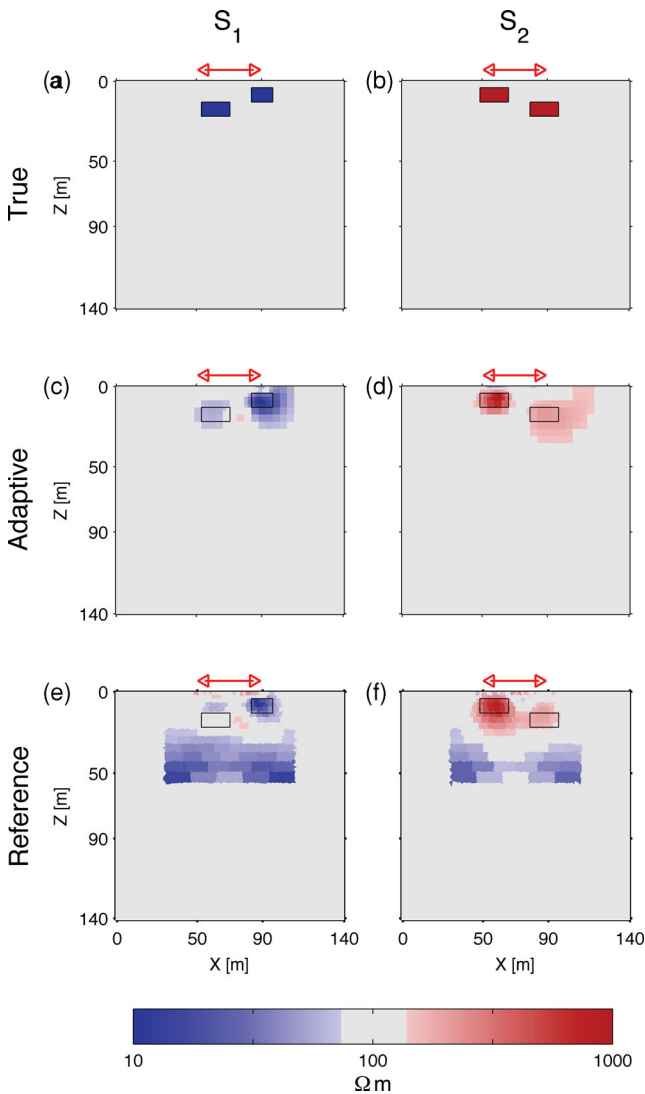


Figure 12. Vertical slices indicated in Fig. 10 through the four block contrasts inversion results. Panels (a) and (b) show the true model, panels (c) and (d) the adaptive wavelet algorithm result and panels (e) and (f) the reference solution. The different results are shown for slice S_1 in (a), (c) and (e) and slice S_2 in (b), (d) and (f) (see Fig. 10). The contrast positions in each panel are indicated by the black boxes. The red arrows show the position of the electrode array.

that the algorithm is capable of generating parameter meshes in a semi-automated fashion. This is particularly important for non-specialists, who wish to perform ERT. Even for a homogeneous model, it can be quite difficult to predict a good mesh, and in the presence of conductivity anomalies, which are previously unknown, the problem becomes even more complicated.

A model parametrization in terms of wavelets is one out of several options for coarsening/refinement procedures. Conceptually, the closest approach to our methodology is a block parametrization using octrees, as suggested by Haber *et al.* (2007). In fact, due to the requirement that our wavelet trees must be complete, there is a formal equivalence between a Haar wavelet basis and octrees. However, our coarsening and refinement schemes could not be directly applied to octrees. The coarsening scheme depends on the fact that removing a parameter with small cumulative wavelet sensitivity coarsens the grid without affecting the cumulative wavelet

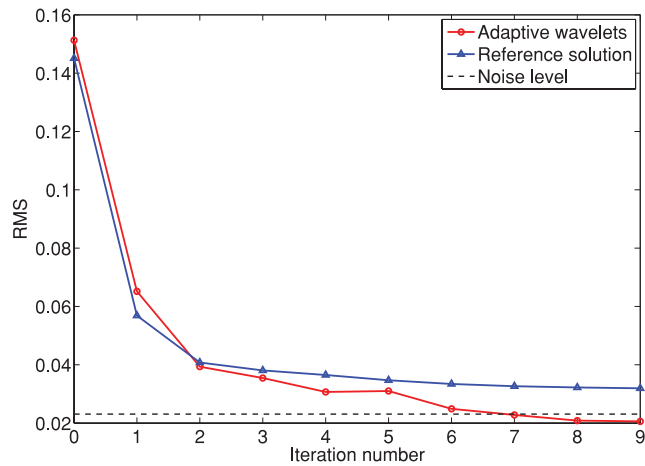


Figure 13. Data rms curves for the reference solution (blue) and the adaptive wavelet solution (red). The dashed line represents the noise level. The initial error is different even though both start with a homogeneous model. This is due to the 2 per cent Gaussian random noises added to each of the ‘observed’ data sets.

sensitivities of the remaining parameters. For octrees, a coarsening would lead to reshaping the parameters in the affected region and hence to different ‘importance values’. The refinement scheme we use would not work because it is by its very design tied to wavelets (see Appendix and Cohen *et al.* 2003a).

In this study, we have applied the adaptive wavelet parametrization to ERT. Because the methodology does not explicitly depend on the governing differential equations that describe the forward problem, it should be straightforward to adapt the technology to other tomographic inversion problems.

ACKNOWLEDGMENTS

We thank Stewart Greenhalgh, Thomas Günther, the editor Mark Everett and an anonymous reviewer for their helpful comments that improved the quality of the paper. Furthermore we thank Wolfgang Dahmen. This work was supported by the Swiss National Science Foundation.

REFERENCES

- Ajo-Franklin, J., Urban, J. & Harris, J., 2006. Using resolution-constrained adaptive meshes for traveltimes tomography, *J. seism. Explor.*, **14**(4), 371–392.
- Ascher, U. & Haber, E., 2001. Grid refinement and scaling for distributed parameter estimation problems, *Inverse Probl.*, **17**(3), 571–590.
- Bijwaard, H., Spakman, W. & Engdahl, E., 1998. Closing the gap between regional and global travel time tomography, *J. geophys. Res.-Sol. Earth*, **103**(B12), 30 055–30 078.
- Blome, M., 2009. Efficient measurement and data inversion strategies for large scale geoelectric surveys, *PhD thesis*, ETH Zurich.
- Blome, M., Maurer, H. & Schmidt, K., 2009. Advances in three-dimensional geoelectric forward solver techniques, *Geophys. J. Int.*, **176**(3), 740–752.
- Blome, M., Maurer, H., Hertrich, M. & Greenhalgh, S., 2010. Experimental design of parallel 3d geoelectric measurements, in *Proceedings of the EAGE Near Surface meeting Zurich*, Switzerland.
- Blome, M., Maurer, H. & Greenhalgh, S., 2011. Geoelectric experimental design: efficient acquisition and exploitation of complete pole-bipole data sets, *Geophysics*, **76**(1), F15–F26.
- Bohm, G. & Vesnaver, A., 1999. In quest of the grid, *Geophysics*, **64**(4), 1116–1125.

- Brislawn, C., Bradley, J., Onyshczak, R. & Hopper, T., 1996. The FBI compression standard for digitized fingerprint images, *Proc. SPIE*, **2847**, doi.org/10.1117/12.258243.
- Chiao, L. & Kuo, B., 2001. Multiscale seismic tomography, *Geophys. J. Int.*, **145**(2), 517–527.
- Cohen, A., Dahmen, W. & DeVore, R., 2001. Adaptive wavelet methods for elliptic operator equations: convergence rates, *Math. Comput.*, **70**(233), 27–75.
- Cohen, A., Dahmen, W. & DeVore, R., 2003a. Sparse evaluation of compositions of functions using multiscale expansions, *SIAM J. Math. Anal.*, **35**(2), 279–303.
- Cohen, A., Dahmen, W. & DeVore, R., 2003b. Adaptive wavelet schemes for nonlinear variational problems, *SIAM J. Numer. Anal.*, **41**(5), 1785–1823.
- Cohen, A., Hoffmann, M. & Reiss, M., 2004. Adaptive wavelet galerkin methods for linear inverse problems, *SIAM J. Numer. Anal.*, **42**(4), 1479–1501.
- Cohen, A., Dahmen, W. & DeVore, R., 2009. Compressed sensing and best k-term approximation, *J. Am. Math. Soc.*, **22**(1), 211–231.
- Curtis, A. & Snieder, R., 1997. Reconditioning inverse problems using the genetic algorithm and revised parameterization, *Geophysics*, **62**(5), 1524–1532.
- Daubechies, I., 1992. *Ten Lectures on Wavelets (CBMS - NSF Regional Conference Series in Applied Mathematics)*, SIAM, Philadelphia, PA.
- Daubechies, I., 1996. Where do wavelets come from? - a personal point of view, in *Proceedings of the IEEE Special Issue on Wavelets*, Vol. 84 (no. 4), pp. 510–513, doi:10.1109/5.488696.
- Daubechies, I., Fornasier, M. & Loris, I., 2008. Accelerated projected gradient method for linear inverse problems with sparsity constraints, *J. Fourier Anal. Appl.*, **14**(5-6), 764–792.
- Dey, A. & Morrison, H., 1979a. Resistivity modeling for arbitrarily shaped 2-dimensional structures, *Geophys. Prospect.*, **27**(1), 106–136.
- Dey, A. & Morrison, H., 1979b. Resistivity modeling for arbitrarily shaped 3-dimensional structures, *Geophysics*, **44**(4), 753–780.
- Donoho, D., 1995. Nonlinear solution of linear inverse problems by wavelet-vaguelette decomposition, *Appl. Comput. Harmon. A.*, **2**(2), 101–126.
- Haber, E., Heldmann, S. & Ascher, U., 2007. Adaptive finite volume method for distributed non-smooth parameter identification, *Inverse Probl.*, **23**(4), 1659–1676.
- Holschneider, M., 1995. *Wavelets: An Analysis Tool*, Oxford University Press, New York, NY.
- Kim, M., Kim, S., Lee, K. & Kim, K., 2004. Improvement of the electrical impedance tomographic image for the two-phase system with adaptive element grouping technique, *Meas. Sci. Technol.*, **15**(7), 1391–1401.
- Loris, I., 2009. On the performance of algorithms for the minimization of $l(1)$ -penalized functionals, *Inverse Probl.*, **25**(3), doi:10.1088/0266-5611/25/3/035008.
- Loris, I., Nolet, G., Daubechies, I. & Dahlen, F., 2007. Tomographic inversion using $l(1)$ -norm regularization of wavelet coefficients, *Geophys. J. Int.*, **170**(1), 359–370.
- Maurer, H. & Boerner, D., 1999. Combination of correlated parameters - constructing well-posed problems, in *Symposium 3DEM2*, pp. 140–143, Salt Lake City, Utah.
- Maurer, H. & Friedel, S., 2006. Outer-space sensitivities in geoelectrical tomography, *Geophysics*, **71**(3), G93–G96.
- Maurer, H., Holliger, K. & Boerner, D., 1998. Stochastic regularization: smoothness or similarity?, *Geophys. Res. Lett.*, **25**(15), 2889–2892.
- Maurer, H., Curtis, A. & Boerner, D., 2010. Recent advances in optimized geophysical survey design, *Geophysics*, **75**(5), A177–A194.
- Menke, W., 1989. *Geophysical Data Analysis: Discrete Inverse Theory*, Revised edition, Academic Press, San Diego, CA.
- Michellini, A., 1995. An adaptive-grid formalism for travel-time tomography, *Geophys. J. Int.*, **121**(2), 489–510.
- Molinari, M., Blott, B., Cox, S. & Daniell, G., 2002. Optimal imaging with adaptive mesh refinement in electrical impedance tomography, *Physiol. Meas.*, **23**(1), 121–128.
- Nolet, G. & Montelli, R., 2005. Optimal parametrization of tomographic models, *Geophys. J. Int.*, **161**(2), 365–372.
- Pessel, M. & Gibert, D., 2003. Multiscale electrical impedance tomography, *J. geophys. Res.*, **108**(B1), doi:10.1029/2001JB000233.
- Plattner, A., Maurer, H., Vorloeper, J. & Dahmen, W., 2010. Three-dimensional geoelectric modelling with optimal work/accuracy rate using an adaptive wavelet algorithm, *Geophys. J. Int.*, **182**(2), 741–752.
- Rantala, M., Vanska, S., Jarvenpaa, S., Kalke, M., Lassas, M., Moberg, J. & Siltanen, S., 2006. Wavelet-based reconstruction for limited-angle x-ray tomography, *IEEE T. Med. Imaging*, **25**(2), 210–217.
- Rücker, C., Günther, T. & Spitzer, K., 2006. Three-dimensional modelling and inversion of dc resistivity data incorporating topography - I. Modelling, *Geophys. J. Int.*, **166**(2), 495–505.
- Sambridge, M. & Faletic, R., 2003. Adaptive whole Earth tomography, *Geochem. Geophys. Geosy.*, **4**(3), doi:10.1029/2001GC000213.
- Simons, F. et al., 2011. Solving or resolving global tomographic models with spherical wavelets, and the scale and sparsity of seismic heterogeneity, *Geophys. J. Int.*, **187**(2), 969–988.
- Spakman, W. & Bijwaard, H., 2001. Optimization of cell parameterizations for tomographic inverse problems, *Pure appl. Geophys.*, **158**(8), 1401–1423.
- Spitzer, K., 1995. A 3-d finite difference algorithm for DC resistivity modelling using conjugate-gradient methods, *Geophys. J. Int.*, **123**(3), 903–914.
- Stummer, P., Maurer, H. & Green, A., 2004. Experimental design: electrical resistivity data sets that provide optimum subsurface information, *Geophysics*, **69**(1), 120–139.
- Tarantola, A., 2005. *Inverse Problem Theory*, SIAM, Philadelphia, PA.
- Tarantola, A. & Valette, B., 1982. Generalized non-linear inverse problems solved using the least-squares criterion, *Rev. Geophys.*, **20**(2), 219–232.
- Telford, W., Geldart, L. & Sheriff, R., 1990. *Applied Geophysics*, Cambridge University Press, Cambridge.
- Tikhotsky, S. & Achauer, U., 2008. Inversion of controlled-source seismic tomography and gravity data with the self-adaptive wavelet parametrization of velocities and interfaces, *Geophys. J. Int.*, **172**(2), 619–630.
- Trinks, I., Singh, S., Chapman, C., Barton, P., Bosch, M. & Cherrett, A., 2005. Adaptive travelttime tomography of densely sampled seismic data, *Geophys. J. Int.*, **160**(3), 925–938.
- Vorloeper, J., 2010. *Adaptive Wavelet Methoden für Operator Gleichungen – Quantitative Analyse und Softwarekonzepte*, VDI Verlag GmbH, Düsseldorf.
- Weber, Z., 2001. Optimizing model parameterization in 2d linearized seismic travelttime tomography, *Phys. Earth planet. Inter.*, **124**(1-2), 33–43.
- Zhang, H. & Thurber, C., 2005. Adaptive mesh seismic tomography based on tetrahedral and Voronoi diagrams: application to Parkfield, California, *J. geophys. Res.*, **110**(B4), B04303, doi:10.1029/2004JB003186.
- Zhou, B. & Greenhalgh, S., 1999. Explicit expressions and numerical calculations for the Fréchet and second derivatives in 2.5D Helmholtz equation inversion, *Geophys. Prospect.*, **47**(4), 443–468.
- Zhou, B. & Greenhalgh, S., 2001. Finite element three-dimensional direct current resistivity modelling: accuracy and efficiency considerations, *Geophys. J. Int.*, **145**(3), 679–688.

APPENDIX A: MODEL PARAMETRIZATION REFINEMENT

The adaptive refinement procedure is described in Cohen *et al.* (2003a) and in more detail in Vorloeper (2010). It considers a map F , which transforms the wavelet coefficients of an input function u into the wavelet coefficients of the resulting function w

$$w = F(u). \quad (A1)$$

This map must satisfy the Lipschitz continuity assumption

$$\|F(u) - F(u')\| \leq C_1 \|u - u'\|, \quad (A2)$$

where u' is another (arbitrary) input function in its wavelet decomposition and C_1 is a non-decreasing positive function of $\sup(\|u\|, \|u'\|)$. A second requirement for F is the so-called wavelet

compressibility, which imposes constraints on the relationship between the coefficients of \mathbf{u} and \mathbf{w} (eq. A1).

$$|w_i| \leq C_2 \sup_{\{\phi_j | \phi_j \cap \phi_i \neq \emptyset\}} (|u_j| \cdot 2^{-c(\text{level}(\phi_i) - \text{level}(\phi_j))}). \quad (\text{A3})$$

To satisfy the wavelet compressibility, small scale details in the function u are not allowed to strongly influence large scale details in the function w . Conversely, large scale details in the function u are not allowed to strongly influence small scale details in the function w . Similar to C_1 , also C_2 is a non-decreasing positive function of $\|u\|$.

For the adaptive wavelet forward modelling algorithm in Cohen *et al.* (2003b), these two assumptions are satisfied and hence the refinement procedure is guaranteed to lead to an optimal work/accuracy rate. For the inversion model parametrization no corresponding proofs exist. Here, we assume the existence of a map \mathbf{F} that relates what we call the cumulative point sensitivities to the model parametrization. The ‘cumulative point sensitivities’ $C_p(r)$ are the sum of the absolute values of the $g_{ij}(r)$ from eq. (3)

$$C_p(r) := \sum_{ij} |g_{ij}(r)|. \quad (\text{A4})$$

Hence we use the wavelet decomposition of $C_p(r)$ as \mathbf{u} and the wavelet decomposition of the subsurface conductivity as \mathbf{w} . The refinement algorithm from Cohen *et al.* (2003a), which we roughly describe later, is particularly interesting because it does not depend on explicit knowledge of the function \mathbf{F} but only on the wavelet compressibility value c in eq. (A3). We make use of this refinement algorithm by choosing an appropriate value for c . The output is a wavelet tree, which we then append to the currently used wavelet basis.

We are introducing the cumulative point sensitivities because the cumulative wavelet sensitivities (eq. 14), employed for the coarsening procedure, are not suitable. They describe the resolvability of a

particular model parameter, but they are unable to characterize the sensitivity at a particular location in the subsurface. The wavelet reconstructions for the cumulative point sensitivities can be easily obtained by performing fast wavelet transforms of the rows of \tilde{G} .

In the following, we give a summary of the application of the refinement procedure described in Cohen *et al.* (2003a) to the wavelet decomposition of the cumulative point sensitivities. Consider the hierarchical tree formed by the cumulative point sensitivity wavelet coefficients \mathcal{T} . For identifying the importance of the individual coefficients of this tree, we apply a series of coarsening procedures, whereby the elimination threshold is gradually increased. This leads to a sequence of coarsened trees $\mathcal{T}_0, \dots, \mathcal{T}_J$, where \mathcal{T}_j is defined as the index set of the result of a tree coarsening of $C_p(r)$ by $2^j \varepsilon' / (1 + j)$ followed by a tree expansion assuring that $\mathcal{T}_{j-1} \subseteq \mathcal{T}_j$. This procedure is described in detail in Cohen *et al.* (2003a). The trees are related as

$$\mathcal{T}_J \subseteq \mathcal{T}_{J-1} \subseteq \dots \subseteq \mathcal{T}_1 \subseteq \mathcal{T}_0. \quad (\text{A5})$$

Next, the differences Δ_j between the \mathcal{T}_j and \mathcal{T}_{j+1} , where $j = 0, \dots, J - 1$ are formed

$$\Delta_j := \mathcal{T}_j \setminus \mathcal{T}_{j+1}. \quad (\text{A6})$$

The differences Δ_j can be interpreted as ‘importance classes’ and the refinement of the tree is governed by these importance classes. The algorithm can be written as follows

```

For each  $\phi \in \mathcal{T}_0$ 
  Set  $j :=$  index of importance class of  $\phi$  and  $l :=$  level of  $\phi$ 
  Add all intersecting wavelets with levels  $l$  to  $l + j / (c + \text{dim} / 2)$ 
end

```

Here, dim is the dimension of the problem, in our case $\text{dim} = 3$ and c is the wavelet compressibility value (eq. A3). In our numerical experiments we have chosen $c = 6$.